BAMS
Article

Pinned Clouds over Industrial Sources of Heat during TRACER

Rusen Öktem,[a,b] Scott E. Giangrande,[c] and David M. Romps[a,b]

KEYWORDS:
Atmosphere;
Convective clouds;
Boundary layer;
Cumulus clouds;
Heat islands

ABSTRACT: An analysis of stereo-camera data from the Tracking Aerosol Convection Interactions Experiment (TRACER) campaign in Houston, Texas, reveals the existence of pinned clouds sitting atop industrial heat sources. These are not plumes of vapor and condensate emanating from stacks: The pinned shallow cumuli have cloud bases at about the lifting condensation of near-surface air. On many mornings, the pinned clouds are the only shallow cumuli in the field of view of the stereo cameras, persisting by themselves for at least an hour. On those mornings, the lower atmosphere straddles the boundary between stable and unstable, and the waste heat from industrial facilities is able to pin moist convection overhead. When solar heating of the surface becomes sufficient later in the morning, those mornings transition to having widespread shallow moist convection. Occurring within the field of view of the stereo cameras and other TRACER instruments, these pinned clouds represent steady plume-like moist convection triggered by known heat sources in a well-characterized atmosphere, making them a rich target for further study.

SIGNIFICANCE STATEMENT: This article introduces steady-state cumulus clouds observed during the Tracking Aerosol Convection Interactions Experiment (TRACER) campaign that were pinned to industrial heat sources. These pinned clouds were present in the early morning only when conditions were primed for moist convection, but for which there was not yet enough solar heating to trigger widespread convection. They persist in a statistical steady state and therefore provide a natural setting to explore the mechanisms controlling convective dynamics, which play a central role in Earth's atmospheric circulation and radiative balance.

DOI: 10.1175/BAMS-D-25-0158.1

Corresponding author: Rusen Öktem, rusenoktem@berkeley.edu

Manuscript received 10 June 2025, in final form 24 October 2025, accepted 8 November 2025

AFFILIATIONS: [a] Department of Earth and Planetary Science, University of California, Berkeley, Berkeley, California; [b] Climate and Ecosystem Sciences Division, Lawrence Berkeley National Laboratory, Berkeley, California; [c] Environmental Science and Technologies Department, Brookhaven National Laboratory, Upton, New York

1. Introduction

The U.S. Department of Energy's (DOE) Atmospheric Radiation Measurement (ARM) deployed instruments from the first ARM Mobile Facility (AMF1) (Ackerman and Stokes 2003; Mather and Voyles 2013; Miller et al. 2016) to the greater Houston, Texas, area to support the Tracking Aerosol Convection Interactions Experiment (TRACER) field campaign from 1 October 2021 through 30 September 2022 (Jensen et al. 2023). The main objective of the campaign was to study moist convection in the presence of diverse sources of aerosols, both anthropogenic and natural. Over the course of the campaign, data were collected at fixed and mobile platforms to characterize aerosols, air quality, deep convective systems, and atmospheric–boundary layer processes including sea-breeze circulations (Wang et al. 2022; Klein et al. 2023; Mages et al. 2025; Lamer et al. 2024; Rapp et al. 2024; Wang et al. 2024; Jensen et al. 2025; Deng et al. 2025; Subba et al. 2025).

The TRACER campaign offered an opportunity to study the complicated interactions between moist convection and heterogeneous environmental conditions. Being close to the coast and Galveston Bay, Houston's summers experience onshore flow and sea-breeze-forced convection, whereas its winters are mainly affected by large-scale synoptic systems (Jensen et al. 2023; Sharma et al. 2024). In addition, the main AMF1 site (M1) was stationed at La Porte Airport, which is within a few kilometers of extensive chemical manufacturing, petroleum refining, and industrial gas-production facilities.

Stereo cameras (STEREOCAM; Romps and Öktem 2020) were among the many instruments positioned in Houston during the TRACER campaign to collect data over the M1 site. The setup consisted of a pair of surveillance cameras at the edge of Galveston Bay in the neighborhood of Bay Oaks Harbor in Baytown. The cameras faced west over the bay toward Morgan's Point and La Porte. Taking synchronized photographs at 20-s intervals during the daytime, the setup generated photographs, time-lapse movies, and the Point Cloud of Cloud Points (PCCP) product (Romps and Öktem 2020; Gaustad and Öktem 2022). The PCCP product is a collection of three-dimensional (3D) cloud-feature positions, at 20-s intervals, that are generated by matching the same cloud feature in time-synchronized pictures and applying stereo reconstruction (Öktem et al. 2014; Romps 2024).

Visual inspection of the photographs revealed, on some of the days, individual shallow cumulus clouds that seemed pinned to particular locations. These "pinned clouds" would begin before or around sunrise and would typically remain steady for at least 1 h until the onset of widespread shallow cumulus or congestus clouds. Analysis of their 3D coordinates from the PCCP product indicated that these pinned clouds were located atop a number of gas-fired power plants.

It is important to note that these pinned clouds are *not* plumes of vapor and condensate emanating from the tops of stacks. Rather than forming at the tops of stacks, we will show in section 2 that the clouds form near the lifting condensation level (LCL) of the ambient near-surface air. Thus, the pinned clouds are ordinary cumulus clouds. They are easily identified in early-morning conditions that are primed for moist convection, but for which there is not yet enough solar heating to spark widespread convection. In these early-morning environments, the heat from the stacks provides the nudge needed to initiate and pin the clouds to their locations. The steady-state nature of pinned clouds presents something of a “golden case” for the study of moist convection, with well-characterized environmental conditions from AMF1, known nudges from reported stack heat output, and unobstructed observations from the stereo cameras. These pinned clouds provide an opportunity to test our understanding of the mechanisms controlling convective dynamics, which play a central role in Earth’s atmospheric circulation and radiative balance.

Here, we describe the characteristics of TRACER’s pinned clouds, and we explain the conditions favoring or inhibiting their formation. In section 2, we describe the instrument setup and the measurements collected during the campaign that are used to characterize the pinned clouds. We investigate the characteristics of these clouds and analyze the meteorological conditions favoring or inhibiting them in section 3. We summarize our findings in section 4 and present our conclusions in section 5.

2. Instruments and data

Figure 1 shows a map covering the main campaign site (M1), the stereo cameras, and the industrial plants triggering pinned clouds. The blue circles labeled as P1 and P2 represent the Air Liquide Bayport cogeneration plant (P1) and the location of the Linde HyCO and Clear Lake Petrochemical (Celanese Ltd and Arkema Inc) plants (P2). The pinned clouds associated with those plants are often distinguishable from the background and from each other. The morning winds are usually from the south, which tends to push those clouds further into the center of the field of view, facilitating an analysis. On the other hand, the pinned clouds associated with the plants labeled P3–P6 are nearly colinear with the line of sight from the cameras, which causes them to overlap in the photographs, making them more difficult to distinguish from each other. Furthermore, the southerly winds tend to push those clouds toward (and sometimes off the edge of) the right-most field of view of one or both of the cameras, hampering the stereo reconstruction. For these reasons, our focus is on the pinned clouds at P1 and P2.

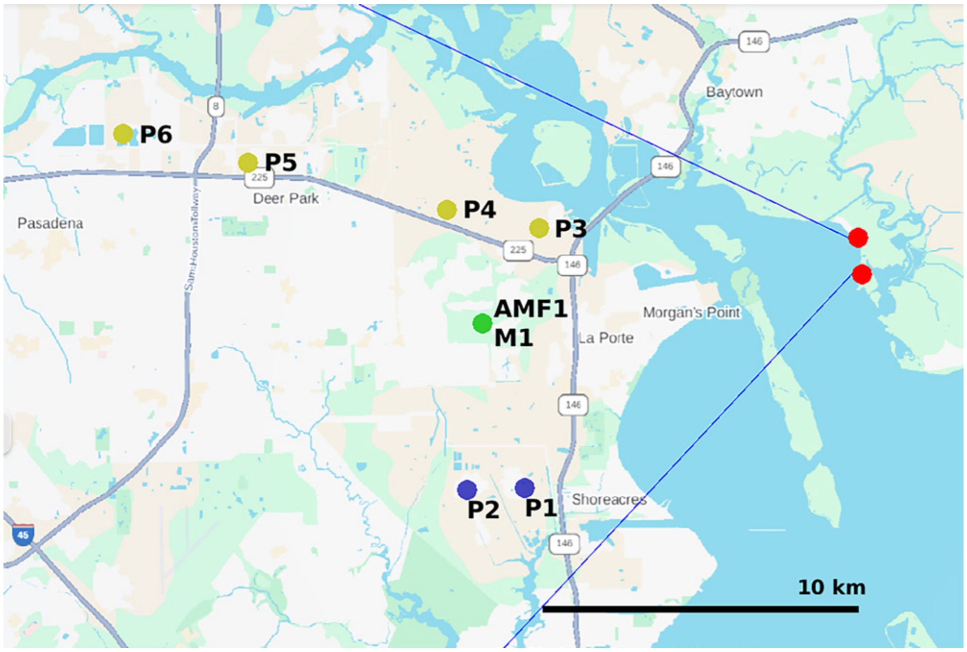

Fig. 1. Map of selected locations during the TRACER campaign, including the M1 site (green circle), stereo cameras (red circles), industrial heat sources that induce pinned clouds (blue and yellow circles), and the approximate northern and southern limits of the stereo cameras’ common field of view (blue lines).

Throughout, we will define local time (LT) to be coordinated universal time minus 5 h (UTC − 5), which corresponds to central daylight time (CDT). All of the observed occurrences of pinned clouds were in the months of May–October, which is when the central time zone observes daylight-saving time, making CDT a natural choice for LT. For simplicity, we will define LT to be UTC − 5 regardless of the time of year. This study will present times using a 24-h notation (e.g., 0230 LT instead of 2:30 a.m. LT, and 1430 LT instead of 2:30 p.m. LT).

a. Stereo-camera setup. The two cameras (Netcam SC 5MP with 4.5–13-mm varifocal lens, 1944 × 2592 pixel resolution) of the stereo-camera setup were positioned at (29° 41′ 38.1″N, 94° 56′ 11.9″W) and (29° 41′ 1.1″N, 94° 56′ 8.13″W). Facing west with a 1.1-km separation between them, the cameras had a ~65° horizontal field of view as depicted by the blue lines in Fig. 1. The M1 site was located near the center of this field of view at a distance of ~12 km. The cameras started routine operation on 1 September 2021 and took time synchronized photographs at 20-s intervals during the daytime through 30 September 2022. Those photographs were used to produce two main types of products: time-lapse movies and stereo reconstructions of the cloud features. The stereo reconstructions provide a set of 3D locations of cloud features at every 20-s interval, forming the PCCP (Romps and Öktem 2020). These 3D locations can be used to estimate sizes, heights, speeds, and lifetimes of individual clouds (Romps and Öktem 2015; Romps et al. 2021). For the TRACER campaign, the PCCP product contains data on cloud features up to 13 km above ground level (AGL)[1] within the ~65° horizontal field of view depicted in Fig. 1. The PCCP data are available for 329 out of the 379 days spanning 17 September 2021–30 September 2022[2] (Gaustad and Öktem 2022, PCCP): No PCCP data were generated on 22 days characterized as clear-sky or cirrus-only, 4 days that were overcast or foggy, and 24 days when the cameras had technical issues. Among the days when the Doppler lidar was operating, the stereo cameras were able to characterize the clouds on 344 days using some combination of PCCP data and photographs (which can be used to identify foggy, overcast, clear-sky, and cirrus-only).

b. Radiosondes. Starting at 0030 LT 1 October 2021, the balloon-borne sounding system (SONDE; Keeler et al. 2022) began launching balloons at 6-h intervals from the M1 site. Prior to 1 October 2021, the morning radiosonde launches were sporadic and at irregular times. The radiosonde data contain vertical profiles of both the thermodynamic state of the atmosphere and the horizontal wind speed and direction at 1-s intervals, which correspond to height intervals of ~5 m. Unless otherwise stated, the radiosonde data used here are from the launches at 0630 LT, which is closest to the time the pinned clouds studied here start to form.

c. Doppler lidar. The Doppler lidar (DL; Newsom et al. 2022) is an active remote sensing instrument that provides a Doppler spectra as the raw data. From raw data, range- and time-resolved measurements of the line-of-sight component of air velocity (i.e., radial velocity) and attenuated aerosol backscatter are obtained. The Doppler lidar alternated between a vertically staring mode (lasting 13–15 min) and either a single-pass or double-pass plan-position-indicator (PPI) mode (lasting 1–2 min). For our purposes, we used data from its operation in the vertically staring mode, which provided profiles of vertical air velocity at ~1-s time intervals and 30-m height intervals from 15 to 9585 m AGL.

d. Pinned-cloud dataset. During the TRACER campaign, there were 344 mornings during which the stereo cameras and Doppler lidar were collecting data in the 3-h interval centered

---

[1] Ground level is 8 m above mean sea level.

[2] The cameras started operation on 1 September 2021, but the calibration required for stereo reconstruction was completed on 17 September 2021.

on a 0630 LT radiosonde launch. By visual inspection of the photographs, we identified the presence of pinned clouds over P1 on 28 of those mornings. We discarded eight of those days because the pinned clouds lasted less than 1 h, leaving us with 20 days.

The automatically generated PCCP data are generated by an algorithm that does not rely on a priori information about the clouds' position. Consequently, for a given feature point in one image, the algorithm searches for a matching feature point throughout most of the epipolar line in the paired image. This results in a relatively high number of false positives, which are filtered by postprocessing. Given our focus on the P1 pinned clouds, we have used the general location of P1 as a priori information, allowing the algorithm to focus on smaller segments of the corresponding epipolar lines. This decreased the number of false positives, which allowed for the use of a less-aggressive postprocessing filter, resulting in a higher number of reconstructed points on the pinned clouds. This created a dataset that we will refer to here as Point Cloud of Pinned Cloud Points (PCPCP). Of the 20 days, we were unable to perform satisfactory stereo reconstructions on six of those days due to insufficient sunlight or because the view was obstructed by other shallow clouds. That left 14 days spanning May–September of 2022, which are listed in Table 1.

3. Early morning pinned clouds

Figure 2 shows seasonal climatologies of the diurnal cycle of cloud feature points from the PCCP data. These data span 2214 h in total (~400 000 pairs of photographs) over 359 days from 17 September 2021 through 26 September 2022. The colors represent the number of detected cloud feature points per vertical distance and per time on the average day in the season. Note that stereo reconstruction can be performed only on the identifiable cloud

Table 1. The 14 mornings with pinned clouds selected for study here (out of the original 28) based on data availability and the criterion that the pinned clouds were observed persisting for more than 1 h. For the pinned clouds, the properties listed here include the observed ranges of their CBH and CTH AGL from PCPCP, their morphological type (either a plume or a cloud street), and their start time. Start times marked by an asterisk are when there was enough daylight to begin seeing the pinned clouds; the pinned clouds likely existed prior to these times. The start time marked by a plus sign is when the pinned cloud began, but it briefly coexisted with other nonpinned shallow cumuli; the other shallow cumuli disappeared at 0700 LT. Also listed are the time of onset of widespread cumulus convection (from stereo-camera photographs) and the LCL and wind speeds from the 0630 LT radiosonde (with speeds measured at the pinned clouds' CBH and CTH at the closest available time to 0630 LT).

	Properties of the pinned Cu							
Date	CBH (m)	CTH (m)	Type	Start (LT)	Other Cu Start (LT)	LCL (m)	Wind CBH (m s^{-1})	Wind CTH (m s^{-1})
13 May 2022	450–600	750–900	Street	0630	0900	500	7.9	8.7
2 Jun 2022	350–450	900–1700	Plume	0600*	0930	400	4.1	4.8
10 Jun 2022	250–450	500–850	Street	0600*	0825	200	11.0	10.0
11 Jun 2022	250–350	400–800	Street	0600*	0855	200	11.6	9.1
17 Jun 2022	400–550	1200–2100	Plume	0600*	0850	500	3.7	7.0
18 Jun 2022	300–450	1200–1400	Plume	0600*	0835	400	3.2	4.4
22 Jun 2022	500–600	1700–2150	Plume	0600*	0815	550	1.8	3.9
15 Jul 2022	550–750	1200–1950	Plume	0610*	0830	600	3.9	5.0
16 Jul 2022	400–550	1050–1700	Street	0610*	0820	500	6.3	7.4
26 Jul 2022	550–600	850–1350	Street	0630	0800	600	7.7	6.9
27 Jul 2022	550–650	950–1500	Street	0630*	0820	650	5.7	6.6
9 Aug 2022	750–800	1000–1500	Street	0650^{+}	0820	650	6.4	5.1
27 Aug 2022	300–400	1900–2650	Plume	0630*	0830	400	6.7	3.1
20 Sep 2022	400–450	1400–2250	Plume	0640*	0915	550	2.1	3.6

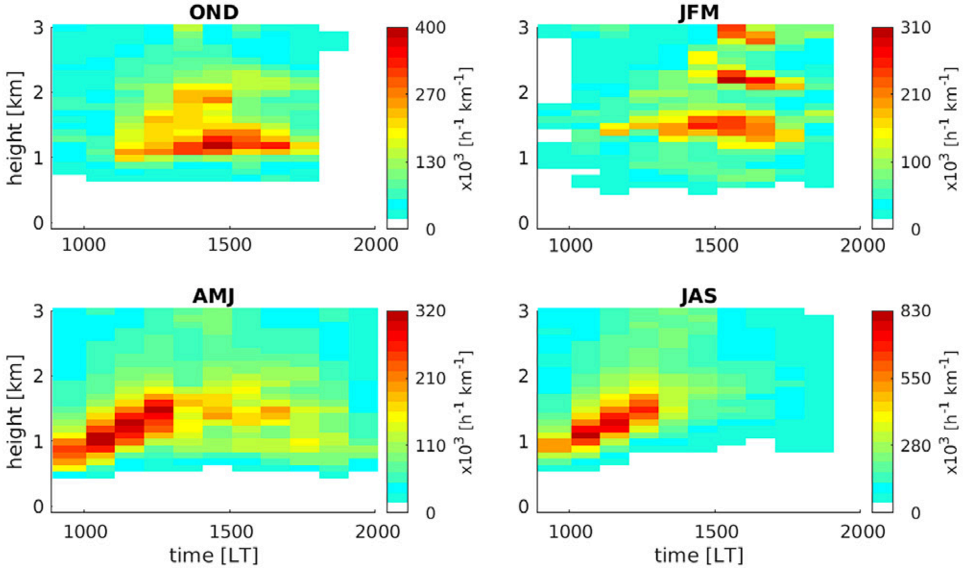

Fig. 2. The average diurnal distribution of cloud feature points in each season, presented as the number of points per vertical distance per time recorded in the PCCP data.

features visible in convective clouds; stratus, altostratus, and cirrus are often not detected by the PCCP algorithm.

Stereo-camera reconstruction is best suited for collecting data from cumulus and isolated cumulonimbus due to their crisp and unobstructed visual features. The higher overall number of cloud points reconstructed in spring and summer reflect the greater prevalence of those types of clouds. It is also notable that, in the fall and winter months, there tends to be few cloud features in the mornings. In the spring and summer, the mornings are dominated by a more regular pattern of shallow cumulus convection: As time progresses from the morning into the early afternoon, the cloud-base height (CBH) and cloud-top height (CTH) increase by several hundreds of meters, associated with the warming of the boundary layer.

a. Cloud-pinning gas plants. Figures 3a, 3c, and 3e show three examples of pinned clouds in the early morning, outlined in white. These pinned clouds form at or before sunrise and remain pinned to the same location for over 2 h. After 2 h, the pinned clouds are surrounded, and often subsumed, by widespread cumulus convection, as shown in Figs. 3b, 3d, and 3f. Furthermore, as is most apparent in Fig. 3a, there are two different heat sources that pin two different clouds. In the case of Fig. 3a, these are the heads of two cloud streets.

The pinned cloud (or street) closer to the cameras is almost always stronger of the two (i.e., more voluminous and with a higher frequency of occurrence). That stronger cloud is pinned to the facility labeled as P1 in Fig. 1. P1 is home to the Air Liquide Bayport Plant, which uses steam methane reforming to generate hydrogen and uses an air separation unit to generate nitrogen, oxygen, and argon. The second pinned cloud can be traced back to the facility labeled as P2 in Fig. 1. P2 is home to the Linde Clear Lake Plant, which also runs steam methane reformers and air separation units, and the Celanese Clear Lake and Arkema Clear Lake Plants, which produce a variety of petrochemicals. All of these facilities are powered by fossil gas, composed primarily of methane or CH_4.

One way to estimate the waste heat from P1 and P2 would be to consider the total amount of fossil gas consumed by the plants, translate that to heat using the enthalpy of combustion, and then subtract the enthalpy exported off site in the form of electricity, steam, and chemical products. The total annual CO_2 equivalent emission from the P1 was 1754 kilotons (kt)

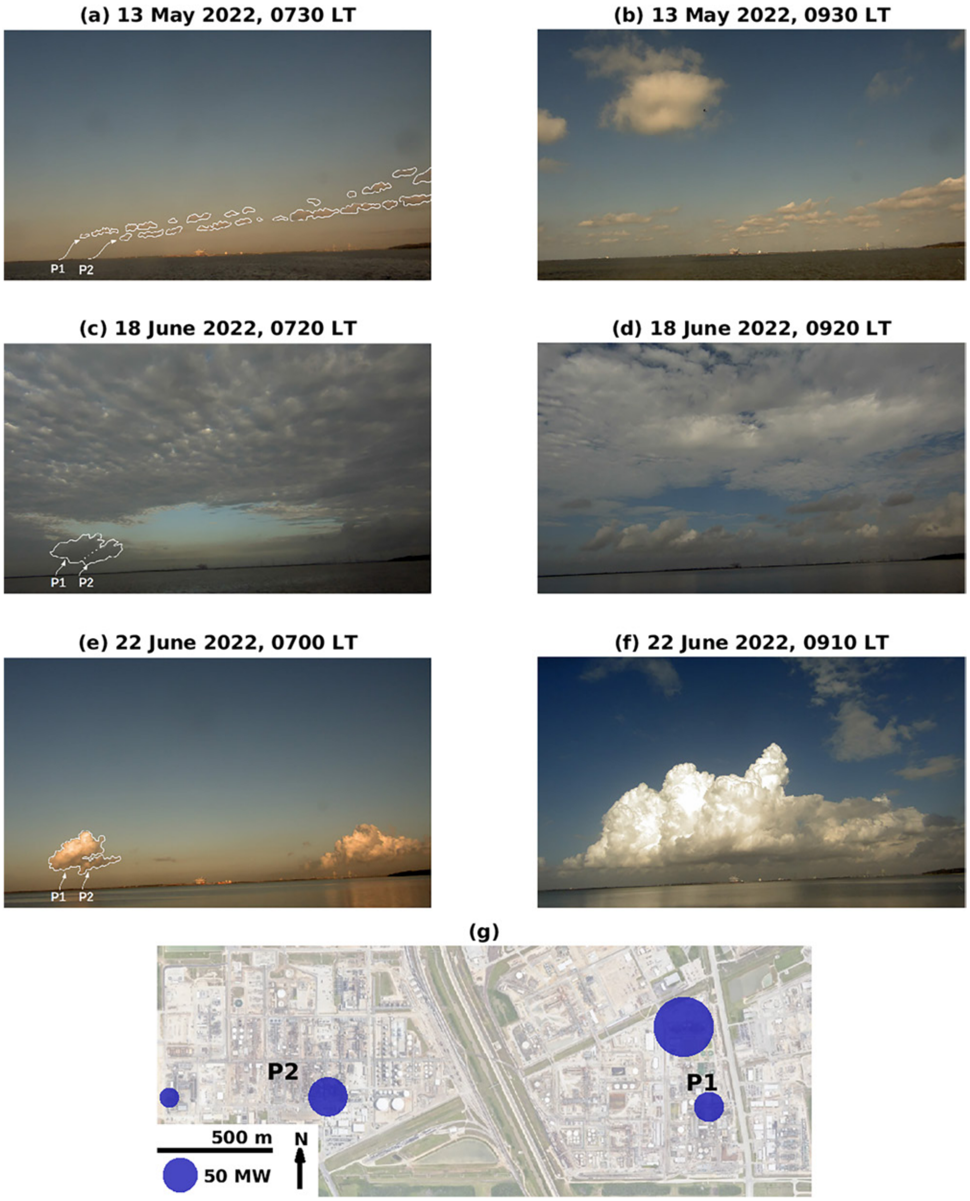

Fig. 3. Examples of pinned clouds and the locations of the pinning heat sources. (a),(c),(e) Pinned clouds captured by the westward-looking northern camera. The outlines of the pinned clouds are highlighted in white. Note that 18 Jun 2022 has an altocumulus deck, which is at 6 km AGL. Note also that there are two pinned clouds per photograph, most visible in (a) and (e); the larger pinned cloud is believed to be triggered by P1 and the smaller by P2. (b),(d),(f) Widespread cumulus clouds start forming after 0900 LT, obfuscating the locations of the pinned clouds. (g) The locations of the heat sources within P1 and P2 are shown with blue circles, with circle area being proportional to the heat emitted.

in 2021, 1949 kt in 2022, and 2017 kt in 2023 (EPA 2025).[3] For comparison, the total annual CO_2 equivalent emissions from P2 was 1609 kt in 2021, 1561 kt in 2022, and 1723 in 2023. From this perspective, P1 and P2 appear to use comparable amounts of fossil gas, but translating this into a release of heat is complicated by two factors. The first is that we do not know how much enthalpy is exported off site. The second is that the use of steam reforming and subsequent utilization of CO and CO_2 in chemical products means that the amount of carbon emitted to the atmosphere as CO_2 is not the same as the amount of carbon consumed in the form of CH_4. Thus, the input of enthalpy in the form of fossil gas cannot be inferred from CO_2 emissions.

---

[3] The total annual CO_2 equivalent emissions can be obtained from the EPA website by searching for the following Greenhouse Gas Reporting Program (GHGRP) IDs: 1000346 for P1; 1006867, 1006797, and 1013977 for P2.

Therefore, we will aggregate estimates of waste heat from stacks using their diameter, effluent temperature, and effluent velocity as reported to the Texas Commission on Environmental Quality.[4] Table 2 lists the stacks at P1 and P2 with more than 5 MW of annually averaged heat output. At P1, the largest source of waste heat comes from four cogeneration power-plant smoke stacks, which, combined, emit 149 MW of annually averaged waste heat. A few hundred meters to the south of that, P1 has boilers BO1–BO4 that emit 27 MW and a reformer stack that emits 11 MW. At P2, the primary source of waste heat is a cluster of three Arkema stacks (east side of P2) and one Celanese stack (west side of P2) that emit 80 MW in total. These clusters of waste heat from stacks are shown in Fig. 3g with circles whose areas are proportional the calculated rate of waste heat. Linde HyCO's stacks, which are to the north of P2, are not shown in the figure because they emit less than 5-MW waste heat.

b. General characteristics of the pinned clouds. By inspection of the stereo-camera photographs, we identified early-morning pinned clouds in October 2021 and in each month from May to September of 2022. The highest frequency of occurrence was in June and July of 2022. Therefore, there appears to be a seasonality in the occurrence of pinned clouds that closely resembles the seasonality of shallow cumulus clouds as illustrated in Fig. 2. Table 1 lists the 14 pinned clouds for which we have 0630 LT radiosonde measurements, DL measurements, and PCPCP data. In Table 1, the start times with an asterisk (i.e., nearly all of them) are the earliest times when there was enough sunlight to detect the clouds in the photographs; their actual start time is likely well before sunrise. These pinned clouds were largely observed in skies that were otherwise clear. The exceptions to that were 2 June and 18 June, when altocumulus was present at 4.5 and 6 km AGL, respectively, and for 9 August, when surface-rooted cumulus clouds were contemporaneous with the pinned cloud until 0700 LT. The "Other Cu Start" column lists the times when widespread cumulus clouds begin to appear. Comparing the start times of the pinned clouds and the widespread clouds in Table 1 shows that the pinned clouds persisted for at least an hour before solar heating was able to form other cumuli.

Table 2. Individual stacks at P1 and P2 that emit at least 5 MW of annually averaged waste heat.

Site	Company	Name	Latitude (°)	Longitude (°)	Diameter (m)	Speed (m s^{-1})	ΔT(K)	Waste heat when on (MW)	Duty cycle	Waste heat average (MW)
P1	Air Liq	CG801	29.6255	95.0473	4.47	22.95	144.04	41	0.98	40
P1	Air Liq	CG802	29.6255	95.0470	4.47	22.95	143.48	41	0.93	38
P1	Air Liq	CG803	29.6255	95.0464	4.47	22.95	144.04	41	0.99	41
P1	Air Liq	CG804	29.6256	95.0462	4.47	22.95	144.04	41	0.71	29
P1	Air Liq	BO1	29.6223	95.0461	2.47	15.18	129.04	8	0.85	7
P1	Air Liq	BO2	29.6226	95.0450	2.47	15.18	129.04	8	0.84	7
P1	Air Liq	BO3	29.6226	95.0450	2.47	15.18	129.04	8	0.69	5
P1	Air Liq	BO4	29.6226	95.0451	2.47	15.18	129.04	8	0.99	8
P1	Air Liq	SMRSTACK	29.6233	95.0468	2.84	19.02	129.04	13	0.81	11
P2	Arkema	66S4ST	29.6230	95.0614	2.83	14.55	784.59	24	1.00	24
P2	Arkema	66S3ST	29.6230	95.0616	2.83	14.55	462.37	20	1.00	20
P2	Arkema	60S108ST	29.6230	95.0632	3.05	16.80	247.93	20	1.00	20
P2	Celanese	REFORM	29.6230	95.0689	3.81	12.19	140.71	16	1.00	16

---

[4] Point source data are obtained from the State of Texas Air Reporting System (STARS) on 14 May 25 for years 2021 and 2022 for the following regulated entities: RN100233998 for P1; RN100239672, RN100227016, and RN104150123 for P2. Data may be subject to revisions and corrections and are a snapshot of the data pulled on the date specified. Emissions data reported by sites met the TCEQ reporting requirements as stated in 30 Texas Administrative Code, Section 101.10, for the given years.

The CBH and CTH columns of Table 1 give the ranges of the CBH and CTH for the pinned clouds. In particular, the range of the CBH values is the range of the 1st percentile of 20 min of PCPCP heights for feature points on the pinned cloud from its start time to the appearance of other cumuli. The range of CTH is defined similarly, but with the 99th percentile. The LCL is calculated using the SONDE measurements and the formulation in Romps (2017) with parcels lifted from near the surface. In particular, we chose to lift from 100 m above mean sea level (MSL) because it was the best among 10–150 m MSL in differentiating between the three types of mornings described in section 3c. We see from Table 1 that the CBH closely matches the LCL. The adjusted R^2 for the relationship between the LCL height and the average CBH height is 0.71 ($p < 10^{-4}$). This confirms that the observed pinned clouds are not stack effluent (in the sense of being formed near the top of the stack from the condensation of emitted water vapor) but are, instead, ordinary cumulus clouds triggered by industrial waste heat in an atmosphere primed for convection (with the priming evident from the fact that widespread shallow cumulus initiated shortly after sunrise in every one of the 14 cases).

c. Conditions favoring pinned clouds. As seen from Table 2, several stacks at both P1 and P2 have duty cycles (fraction of time operating) exceeding 90%, which means the plants emit heat nearly continuously, i.e., nearly every hour of every day of the year. When the boundary layer is very stable, even updrafts nudged by this waste heat are unable to reach the LCL. When the boundary layer is unstable, even updrafts without the benefit of waste heat are able to reach the LCL, and any pinned updrafts are difficult to distinguish from the surrounding convection. We posit, therefore, that only an atmosphere that is weakly stable or weakly unstable allows the pinned clouds to reveal themselves against the backdrop of a lower troposphere otherwise devoid of moist convection.

To investigate this hypothesis, we first sorted the mornings into three categories: those likely containing no surface-rooted convective clouds, those containing pinned clouds only, and those likely containing widespread surface-rooted convective clouds. To perform this sorting, we generated a time–height plot of Doppler lidar radial velocity for each of the mornings, each spanning 3 h centered on 0630 LT and spanning heights from 0 to 2 km AGL. We overlaid cloud points on each of these plots at the time and height where the attenuated backscatter measurement exceeded 6×10^{-5} (m sr)$^{-1}$. These plots revealed the rising thermals and showed the cloud profiles up to 2-km height during the investigated time interval. Figures 4b and 4c show two examples of the generated plots, which have been zoomed in for clarity. Excluding mornings with either fog or only pinned clouds, we shuffled the order of the plots randomly and had two of the coauthors (DR and RO) independently label each plot as either “likely having” or “likely not having” surface-rooted convective clouds. The plots that featured cloud point clusters coupled with thermals rising from the near-surface level up to the cloud base (Fig. 4c) were sorted into the “likely having” category. We then eliminated a handful of mornings for which the two coauthors disagreed or could not assign to either of the categories. This left us with 20 mornings identified as having pinned clouds only, 78 mornings identified as having surface-rooted clouds, and 216 mornings labeled as having no surface-rooted clouds. According to the hypothesis above, these three sets of mornings should have stratifications that are weakly stable or unstable, weakly or strongly unstable, and weakly or strongly stable, respectively.

To quantify the stability of the atmosphere up to the LCL, we need to account for the profile of horizontal winds in addition to the profile of dry static energy. Since these observations are in the early morning, there is no substantial solar heating of the surface to drive convection, but eddies generated by the wind shear can be a source of kinetic energy. For the “lucky” parcels whose trajectories coincide with the ascending branches of those eddies, some of the

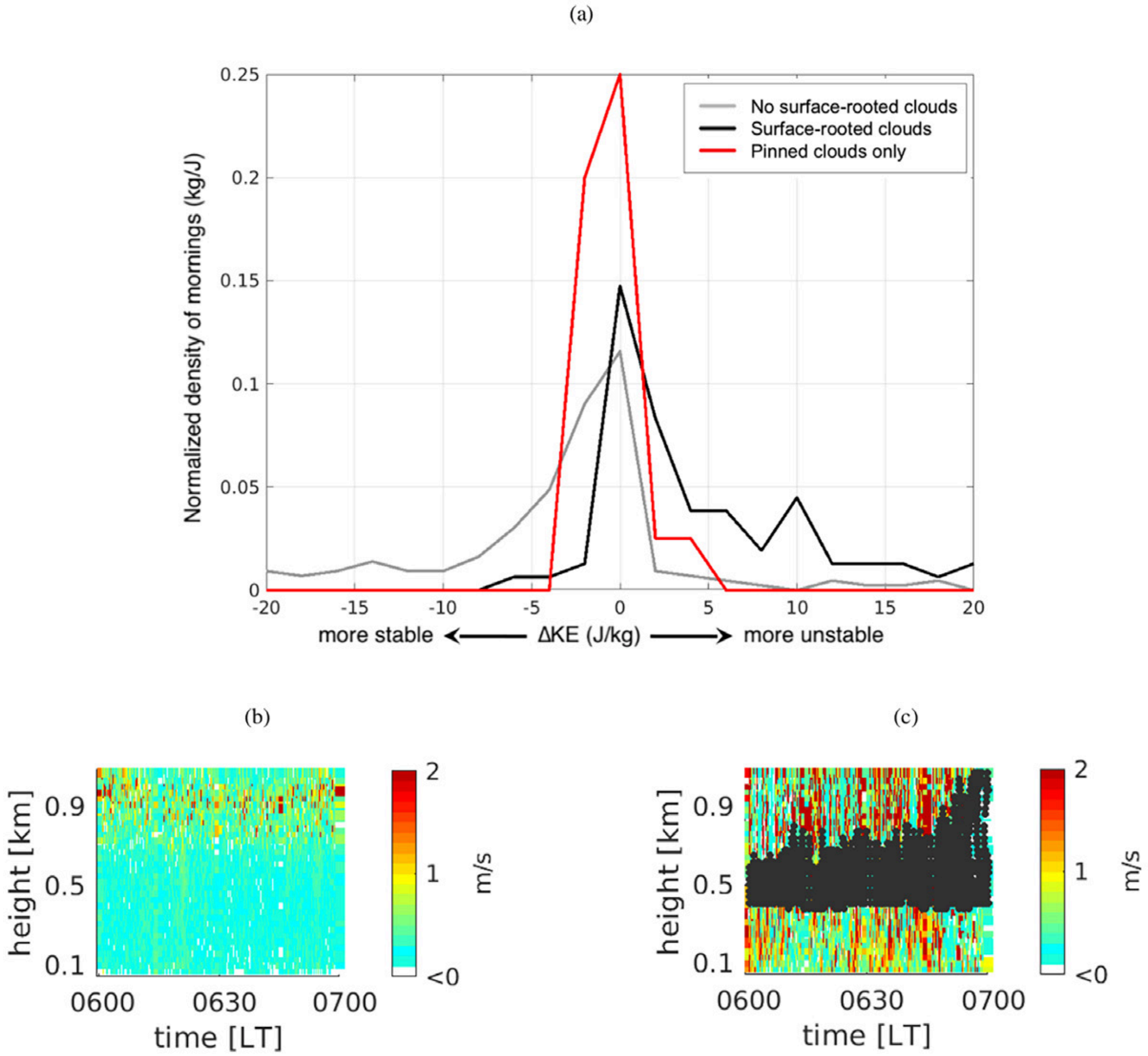

Fig. 4. (a) Distributions of mornings on the summary statistic ΔKE for mornings without observed surface-rooted clouds (gray), mornings with observed surface-rooted clouds (black), and mornings with pinned clouds only (red). Time–height plot of DL radial velocity for two mornings that were classified as (b) "likely not having" or (c) "likely having" surface-rooted convective clouds. The color bars show nonnegative radial velocity capped at 2 m s^{-1}. The dark gray dots illustrate cloud points where attenuated backscatter measurement exceeded 6 × 10^{-5} (m sr)$^{-1}$.

energy in the background wind shear is converted to the kinetic energy of ascent. We can model those "lucky" parcels using

$$\frac{dw}{dz}=\begin{cases} b/w+\beta\left|\frac{\partial \mathbf{u}_h}{\partial z}\right| & z>z_0 \\ \beta\left|\frac{\partial \mathbf{u}_h}{\partial z}\right| & z=z_0 \end{cases}, \tag{1}$$

$$b(z)=\frac{g}{c_pT_e(z)}\left[s_e(z_0)-s_e(z)\right], \tag{2}$$

$$s_e(z)=c_pT_e(z)+gz, \tag{3}$$

where b and w are the parcel's buoyancy and vertical velocity, respectively; $T_e(z)$, $s_e(z)$, and $\mathbf{u}_h(z)$ = [$u_h(z)$, $v_h(z)$] are the atmosphere's profiles of temperature, specific dry static energy, and horizontal wind, respectively; g is the gravitational acceleration; c_p is the specific heat capacity of air at constant pressure; z_0 is taken to be 100 m; and β (a dimensionless number) is the fraction of the wind shear magnitude that is added to the parcel's vertical velocity per vertical distance of ascent (dimensionless).

Equation (1) says that the parcel is accelerated upward by positive buoyancy and by wind shear. We have selected $\beta = 0.6$ as a best-fit value in the sense that it most clearly differentiates between the three types of mornings in the analysis below. Equation (2) defines the parcel's buoyancy in terms of its dry static energy, which is conserved and equals the dry static energy of the atmosphere at its originating height of z_0. Equation (3) gives the definition of dry static energy.

One option would be to assume $w(z_0) = 0$ and then integrate these equations until either w equals zero or z equals the LCL height, whichever comes first. This would provide only a binary prediction: either the parcel reaches the LCL or it does not. Furthermore, that binary prediction would be noisy due to its sensitivity to sampling error (i.e., lack of representativeness) from the radiosonde sounding. Therefore, we use a different approach.

For each morning, we find the smallest nonnegative $w(z_0)$ for which Eqs. (1)–(3) give $w(z) \geq 0$ for all $z \in [z_0, z_{\mathrm{LCL}}]$. If $w(z_0) = 0$ gives nonnegative w from z_0 to the LCL, then no further analysis is conducted. Otherwise, we use a root solver to find the positive value of $w(z_0)$ that ensures w is nonnegative from z_0 to the LCL. As a natural summary statistic, we then calculate the change in the parcel's specific kinetic energy, $\Delta\mathrm{KE} = w^2(z_{\mathrm{LCL}})/2 - w^2(z_0)/2$, for each morning. The more negative (positive) ΔKE is, the more stable (unstable) the boundary layer is.

Figure 4a shows the distributions of mornings on an axis of ΔKE for the three categories of mornings: without observed surface-rooted clouds (shown in gray), with observed surface-rooted clouds (black), and with pinned clouds only (red). As expected, mornings with no surface-rooted clouds are predominantly weakly stable ($\Delta\mathrm{KE} \lesssim 0$) or strongly stable ($\Delta\mathrm{KE} \ll 0$) and mornings with surface-rooted clouds are predominantly weakly unstable ($\Delta\mathrm{KE} \gtrsim 0$) or strongly unstable ($\Delta\mathrm{KE} \gg 0$). Furthermore, mornings with pinned clouds can all be characterized as weakly unstable or weakly stable, i.e., $\Delta\mathrm{KE} \approx 0$. This supports the hypothesis that pinned clouds are visible as stand-alone features when the boundary layer has nearly neutral stratification.

d. Effect of wind on pinned clouds. On 7 of the 14 days, the pinned clouds took the form of a cloud street rather than a vertically developing plume (see Table 1). The CBH wind speed, measured from the radiosonde, was 8.1 ± 2.3 (standard deviation) m s^{-1} on days of a street-like morphology and 3.6 ± 1.3 m s^{-1} on days of a plume-like morphology. The difference in the means of these two sets of wind speeds is statistically significant ($p = 0.001$), indicating a role for the wind speed in setting the morphology of the pinned clouds, as expected.

In Table 1, each pinned cloud identified as a cloud street based on its visual appearance formed when the 0630 LT wind speed at its CBH was above 4.1 m s^{-1} but not more than 11.1 m s^{-1}. The one exception was 27 August 2022, which had a CBH wind speed of 6.7 m s^{-1} at 0630 LT. The cloud that day resembled a cloud street for a short time around 0630 LT, but its shape changed to that of a plume shortly afterward when changes to the wind's speed and direction are detectable from the photographs. From Table 1, we can see that the cloud thickness (inferred from CBH and CTH) also shows a correlation with the CBH wind speed. The lowest pinned-cloud thicknesses (~300 m) tend to occur on the days when the CBH wind speed was above 7 m s^{-1}, and the higher thicknesses of > 1.4 km tend to occur on mornings when the CBH wind speed was below 5 m s^{-1}.

Figure 5a shows a plan view of the density of vertically projected PCPCP feature points (collected from pinned-cloud start to the start of other cumulus clouds, as given in Table 1, and across all 14 days). The axes of the plan view are eastward and northward distances from the M1 site. We see that the highest frequency of cloud points is in the immediate vicinity of P1. This is because P1 is a stronger heat source than P2 and because the pinned cloud over P1 partially obscures P2's pinned cloud. Although the highest frequency of occurrence is around the heat sources, the cloudy air drifts as far away as 10 km (see also Fig. 3a) along the mostly northward wind direction at the cloud-base height. Figure 5b is similar to Fig. 5a except that the axes are the northward distance and the height AGL. This figure shows that pinned clouds can ascend to heights above 2 km AGL. The occurrences of pinned clouds as far north as the stereo cameras (with heights less than 1 km AGL) occurred exclusively on mornings with a CBH wind speed exceeding 7 m s^{-1}.

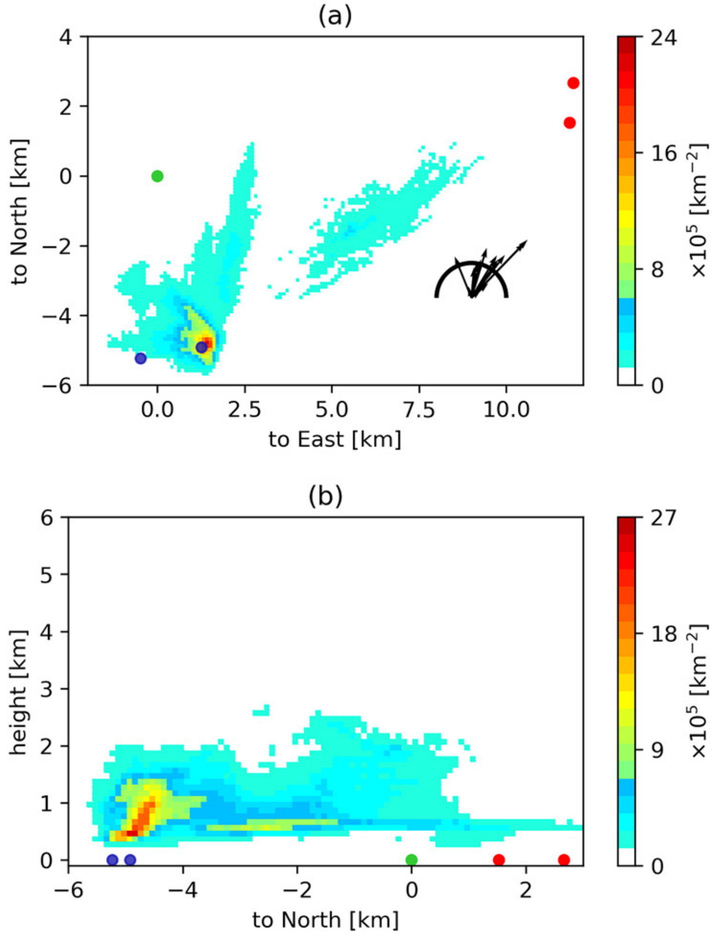

Fig. 5. **(a) Density of PCPCP feature points (collected across all 14 days from pinned-cloud start to the start of other cumulus clouds, as given in Table 1) presented as a plan view with eastward and northward distances given relative to the M1 site. The circles denote the M1 site (green), the stereo cameras (red), and P1 on the right and P2 on the left (blue). The black arrows illustrate the wind direction and wind speed at the CBH obtained from the 0630 LT radiosonde on each of the 14 days; the black circle marks a wind speed of 5 m s^{-1}. (b) As in (a), but the axes are height and northing.**

We can examine the convective motions within pinned clouds by tracking cloud parcels that are distinguishable by eye. Individual cloud features (such as bulges on the clouds) are identified and then tracked between subsequent images starting from their initiation near the cloud base to their dissipation near the cloud top, while recording their pixel positions. With the pixel locations of a cloud parcel identified in a sequence of photograph pairs, stereo reconstruction (Öktem et al. 2014; Romps 2024) provides its trajectory through space and time. Figure 6 shows two such examples: the 13 May 2022 cloud street and the 22 June 2022 plume (see data availability statement for how to access the complete image sequence and dataset of cloud points).

The cloud parcel we tracked in Fig. 6a travels at 8.5 m s^{-1} speed horizontally, which is close to the CBH wind speed of 7.9 m s^{-1}. The vertical development of this cloud street is severely limited, but Fig. 6e shows that some cloud parcels travel over 9 km horizontally before they dissipate. The plan-view PCPCP occurrence fractions of 13 May 2022 in Fig. 6e confirm that the cloud mass drifts along the wind direction, while its horizontally projected width grows from 500 m at a distance of 2 km from the heat sources to a width of 2 km at a distance of 9 km from the heat sources.

In the case of 22 June 2022, the wind speed at the cloud-base height was 1.8 m s^{-1}. Figure 6f shows that this resulted in an upright plume that is mildly tilted by the wind shear.

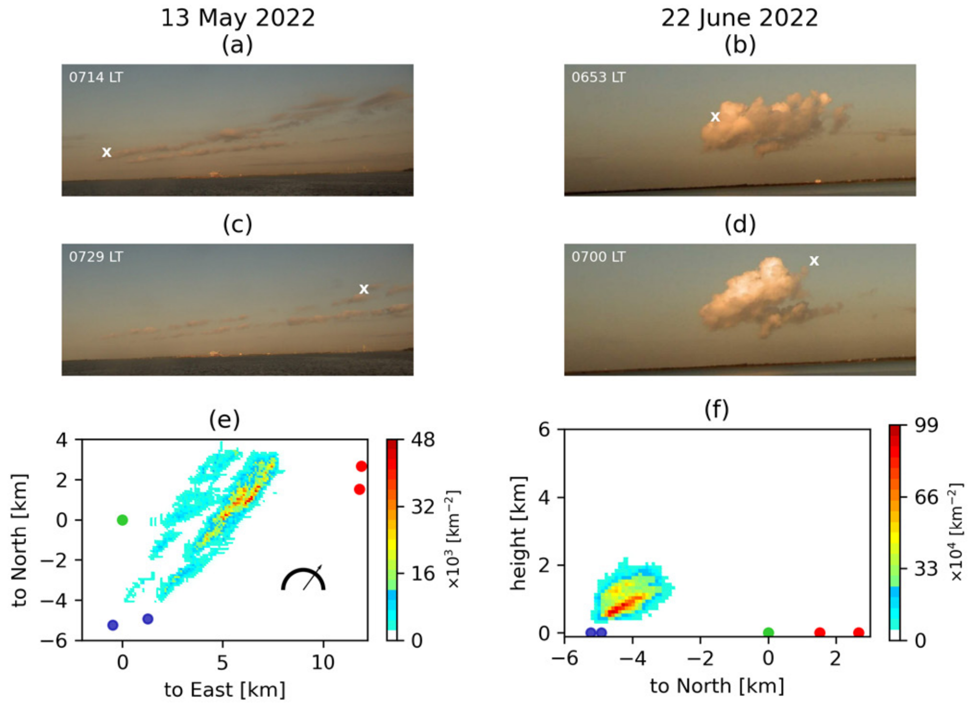

Fig. 6. For 13 May 2022, the location of a selected cloud parcel at (a) 0714 LT and (c) 0729 LT, and (e) density of PCPCP feature points collected from 0630 to 0900 LT plotted against eastward and northward distances from the M1 site. For 22 Jun 2022, the location of a selected cloud parcel at (b) 0653 LT and (d) 0700 LT, and (f) density of PCPCP feature points collected from 0600 to 0815 LT plotted against height AGL and northward distance from the M1 site.

The highest CTH for this case was 2.2 km AGL. Therefore, the plume ascended 1.7 km above the cloud-base height at its peak. We tracked six cloud parcels starting at different times between 0650 and 0750 LT as they traveled up (and drifted ~2.5 km by the horizontal wind) starting from midcloud levels of ~1 km AGL. It was not possible to track the same cloud parcel all the way from the cloud base to the cloud top for this plume, because newly emerging cloud parcels would block them when in the close vicinity of the cloud base. We find that the parcels traveled toward west at ~3 m s^{-1} and north at ~2–3 m s^{-1} (not shown), which are close to the horizontal wind speed at the CTH. The vertical speed of the parcels is estimated in a similar fashion from the data shown in Fig. 7 by fitting a line on the ascending part of the plots, which lasts for approximately 4 min after we started tracking. Averaging the line slopes over six tracks, we calculate the ascent speed as ~3 m s^{-1}. Figure 7 shows that, when the cloud-top height is reached, the cloudy parcels remain at that height for another ~2–5 min before dissipating.

4. Discussion

From the year-long TRACER campaign, we observed two distinct steady-state clouds pinned to two industrial heat sources (two clusters of stacks) on 28 days, of which 14 were suitable for analysis using the atmospheric state and stereo-reconstructed cloud-point measurements. Our findings indicate that, while these pinned clouds are triggered by industrial waste heat, they are otherwise the same as ordinary cumulus clouds: Their occurrence frequency aligns with the seasonal cycle of shallow cumulus clouds, and their average CBH exhibits a statistically significant correlation with the LCL (adjusted $R^2 = 0.71$, $p < 10^{-4}$). Furthermore, the identification of waste heat as the trigger for these clouds is corroborated by the relative sizes of the two pinned clouds: The larger of the two clouds is consistently anchored to the source emitting the greater rate of heat.

Comparing the ΔKE distribution for the set of mornings with pinned clouds only against the one with and the one without widespread surface-rooted clouds, we see that an atmospheric

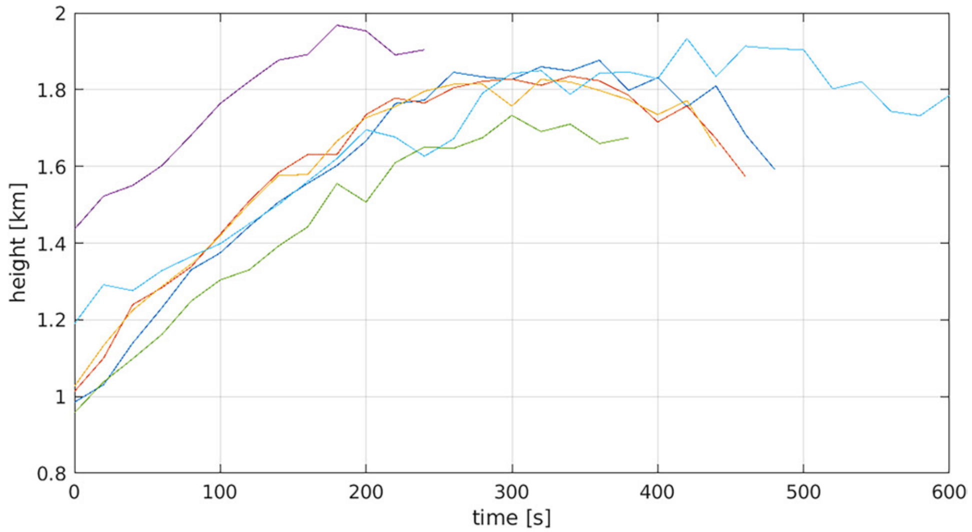

Fig. 7. Time series of height for six cloud parcels selected from the pinned cloud on 22 Jun 2022.

state on the brink of convection ($\Delta KE \approx 0$) favors isolated pinned clouds (see Fig. 4a). Mornings without widespread surface-rooted clouds were predominantly weakly stable ($\Delta KE \lesssim 0$) or strongly stable ($\Delta KE \ll 0$), and mornings with widespread surface-rooted clouds were predominantly weakly unstable ($\Delta KE \gtrsim 0$) or strongly unstable ($\Delta KE \gg 0$).

Of the 14 days with isolated pinned clouds, those pinned clouds formed as cloud streets on half of those days and as vertically developing plumes on the other half (see Table 1). The difference in mean wind speed for those two sets of days is statistically significant ($p = 0.001$), indicating a role for the wind speed in setting the morphology of the pinned clouds. For example, in the case of 22 June 2022, when the wind speed at the CBH was 1.8 m s^{-1}, a mildly tilted upright plume ascended 1.7 km above the cloud-base height at its peak, and drifted ~2.5 km by the horizontal wind. In the case of 13 May 2022, when the CBH wind speed was 7.9 m s^{-1}, the vertical development of the cloud street was severely limited, but the cloud mass drifted 9 km away from the heat sources before dissipating (see Fig. 6).

5. Conclusions

We have demonstrated here the existence of pinned clouds during the TRACER campaign. Furthermore, we have documented the characteristics of those pinned clouds, the industrial heat sources that trigger them, and the conditions in which they form. These clouds present an opportunity to study convective dynamics when the convective trigger is known, the atmosphere is quiescent and well-characterized, and the clouds persist in a steady state. These cases are potentially applicable to validating convective parameterizations and studying the models of plume dynamics that simulate the lofting of wildfire smoke. Only a crude analysis of the dynamics of these pinned clouds has been attempted here, but that analysis confirms that the pinned clouds occur on mornings that are weakly stable or weakly unstable, i.e., primed for moist convection (see Fig. 4a).

Acknowledgments. This research was supported by the U.S. Department of Energy's Atmospheric System Research, an Office of Science Biological and Environmental Research program, under Grant DE-SC0025214. This research was also supported and authored by an employee of Brookhaven Science Associates, LLC, under contract DE-SC0012704 with the U.S. DOE. We acknowledge support from the Atmospheric Radiation Measurement (ARM) program, a user facility of the U.S. DOE Office of Science, sponsored by the Office of Biological and Environmental Research. The publisher by accepting the paper for publication acknowledges that the U.S. Government retains a nonexclusive, paid-up, irrevocable, worldwide license to publish or reproduce the published form of this paper, or allow others to do so, for U.S. Government purposes. We would like to acknowledge Michael Jensen for coordination with the TRACER campaign and Yunyan Zhang and Jingjing Tian for early conversation regarding the pinned clouds. We extend our sincere gratitude to Al Kibbe and Ken Ammons for hosting our stereo-camera setups at their respective properties throughout the duration of the TRACER campaign.

Data availability statement. All ARM datasets used for this study can be downloaded at https://www.arm.gov. DL, SONDE, and PCCP data can be downloaded at https://doi.org/10.5439/1025185, https://doi.org/10.5439/1595321, and https://doi.org/10.5439/1531325. Scripts and data used in generating Figs. 2–7 are accessible at https://github.com/rusenoktem/tracer_pinned_clouds. An additional script to display the tracked cloud features in Figs. 6 and 7 over the complete set of image sequences is also accessible at the same GitHub link.

References

Ackerman, T. P., and G. M. Stokes, 2003: The atmospheric radiation measurement program. *Phys. Today*, **56**, 38–44, https://doi.org/10.1063/1.1554135.

Deng, M., and Coauthors, 2025: A closed bay-breeze circulation and its lifecycle from TRACER with a new orienteering tape recorder diagram. *J. Geophys. Res. Atmos.*, **130**, e2024JD043187, https://doi.org/10.1029/2024JD043187.

EPA, 2025: Facility Level Information on GreenHouse gases Tool (FLIGHT). Accessed 1 March 2025, https://ghgdata.epa.gov/ghgp.

Gaustad, K., and R. Öktem, 2022: Stereo Reconstructed Point Cloud of Cloud Points (PCCP). Atmospheric Radiation Measurement, accessed 7 October 2024, https://doi.org/10.5439/1531325.

Jensen, M. P., and Coauthors, 2023: Tracking Aerosol Convection Interactions Experiment (TRACER) field campaign report. ORNL Tech. Rep. DOE/SC-ARM-23-038, 132 pp., https://doi.org/10.2172/2202672.

——, and Coauthors, 2025: Studying aerosol, clouds, and air quality in the coastal urban environment of southeastern Texas. *Bull. Amer. Meteor. Soc.*, https://doi.org/10.1175/BAMS-D-23-0331.1, in press.

Keeler, E., K. Burk, and J. Kyrouac, 2022: Balloon-Borne Sounding System (SONDEWNPN). Atmospheric Radiation Measurement, accessed 15 August 2024, https://doi.org/10.5439/1595321.

Klein, P., E. Smith, T. Wagner, J. Gibbs, T. Bell, J. Gebauer, M. Spencer, and M. Carney, 2023: TRACER-Coastal Urban Boundary-Layer Interactions with Convection (TRACER-CUBIC) field campaign report. ORNL Tech. Rep. DOE/SC-ARM-23-027, 15 pp., https://doi.org/10.2172/1984939.

Lamer, K., and Coauthors, 2024: Spatially distributed atmospheric boundary layer properties in Houston—A value-added observational dataset. *Sci. Data*, **11**, 661, https://doi.org/10.1038/s41597-024-03477-9.

Mages, Z., P. Kollias, B. P. Treserras, P. Borque, and M. Oue, 2025: Shallow cloud variability in Houston, Texas, during the ESCAPE and TRACER field experiments. *Atmos. Chem. Phys.*, **25**, 6025–6045, https://doi.org/10.5194/acp-25-6025-2025.

Mather, J. H., and J. W. Voyles, 2013: The Arm Climate Research Facility: A review of structure and capabilities. *Bull. Amer. Meteor. Soc.*, **94**, 377–392, https://doi.org/10.1175/BAMS-D-11-00218.1.

Miller, M. A., K. Nitschke, T. P. Ackerman, W. R. Ferrell, N. Hickmon, and M. Ivey, 2016: The ARM mobile facilities. *The Atmospheric Radiation Measurement (ARM) Program: The First 20 Years*, *Meteor. Monogr.*, No. 57, Amer. Meteor. Soc., https://doi.org/10.1175/AMSMONOGRAPHS-D-15-0051.1.

Newsom, R., Y. Shi, and R. Krishnamurthy, 2022: Doppler Lidar (DLFPT). Atmospheric Radiation Measurement, accessed 30 September 2024, https://doi.org/10.5439/1025185.

Öktem, R., Prabhat, J. Lee, A. Thomas, P. Zuidema, and D. M. Romps, 2014: Stereophotogrammetry of oceanic clouds. *J. Atmos. Oceanic Technol.*, **31**, 1482–1501, https://doi.org/10.1175/JTECH-D-13-00224.1.

Rapp, A. D., and Coauthors, 2024: TAMU TRACER: Targeted mobile measurements to isolate the impacts of aerosols and meteorology on deep convection. *Bull. Amer. Meteor. Soc.*, **105**, E1685–E1702, https://doi.org/10.1175/BAMS-D-23-0218.1.

Romps, D. M., 2017: Exact expression for the lifting condensation level. *J. Atmos. Sci.*, **74**, 3891–3900, https://doi.org/10.1175/JAS-D-17-0102.1.

——, 2024: Principles of stereo reconstruction of aerial objects using stationary cameras. *Remote Sens. Lett.*, **15**, 1118–1131, https://doi.org/10.1080/2150704X.2024.2399330.

——, and R. Öktem, 2015: Stereo photogrammetry reveals substantial drag on cloud thermals. *Geophys. Res. Lett.*, **42**, 5051–5057, https://doi.org/10.1002/2015GL064009.

——, and ——, 2020: Point Cloud of Cloud Points (PCCP) value-added product report. ORNL Tech. Rep. DOE/SC-ARM-TR-252, 20 pp., https://doi.org/10.2172/1648150.

——, ——, S. Endo, and A. M. Vogelmann, 2021: On the life cycle of a shallow cumulus cloud: Is it a bubble or plume, active or forced? *J. Atmos. Sci.*, **78**, 2823–2833, https://doi.org/10.1175/JAS-D-20-0361.1.

Sharma, M., A. D. Rapp, C. J. Nowotarski, and S. D. Brooks, 2024: Observed variability in convective cell characteristics and near-storm environments across the sea- and bay-breeze fronts in southeast Texas. *Mon. Wea. Rev.*, **152**, 2419–2441, https://doi.org/10.1175/MWR-D-23-0243.1.

Subba, T., and Coauthors, 2025: Implications of sea breeze circulations on boundary layer aerosols in the southern coastal Texas region. EGUsphere, https://doi.org/10.5194/egusphere-2025-2659.

Wang, D., and Coauthors, 2022: Linking synoptic patterns to cloud properties and local circulations over southeastern Texas. *J. Geophys. Res. Atmos.*, **127**, e2021JD035920, https://doi.org/10.1029/2021JD035920.

——, E. C. Melvin, N. Smith, M. P. Jensen, S. Gupta, A. Abdullah-Smoot, N. Pszeniczny, and T. Hahn, 2024: TRACER perspectives on gulf-breeze and bay-breeze circulations and coastal convection. *Mon. Wea. Rev.*, **152**, 2207–2228, https://doi.org/10.1175/MWR-D-23-0292.1.